Revealing *OOH key intermediates and regulating H_2O_2 photoactivation by surface relaxation of Fenton-like catalysts

Xiaoming Xu[a,b], Yuanming Zhang[a,b], Yong Chen[a,b], Changhao Liu[a,b], Wenjing Wang[a,b], Jiajia Wang[c], Huiting Huang[a,b], Jianyong Feng[a,b], Zhaosheng Li [a,b,1], and Zhigang Zou[a,b]

Zhaosheng Li
Email: zsli@nju.edu.cn.

This PDF file includes:

Supplementary text
Figures S1 to S25 (not allowed for Brief Reports)
Tables S1 to S3 (not allowed for Brief Reports)

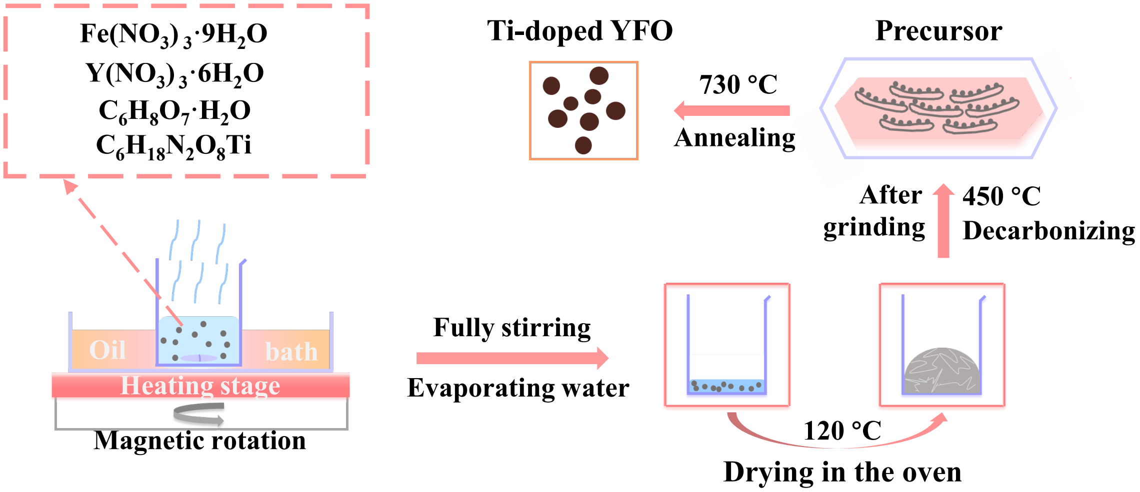

Fig. S1. Schematic illustration of the preparation process of YFeO$_3$.

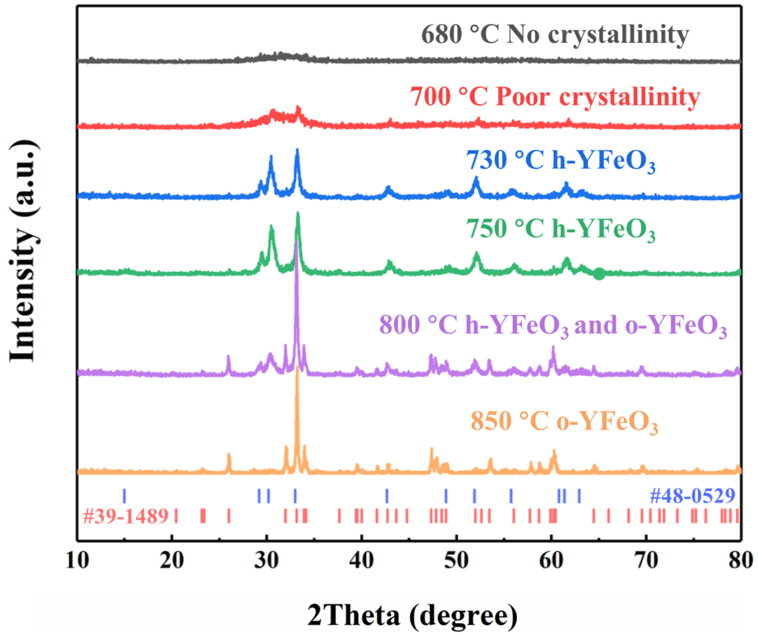

Fig. S2. XRD patterns of $YFeO_3$ after the treatment at different temperatures.

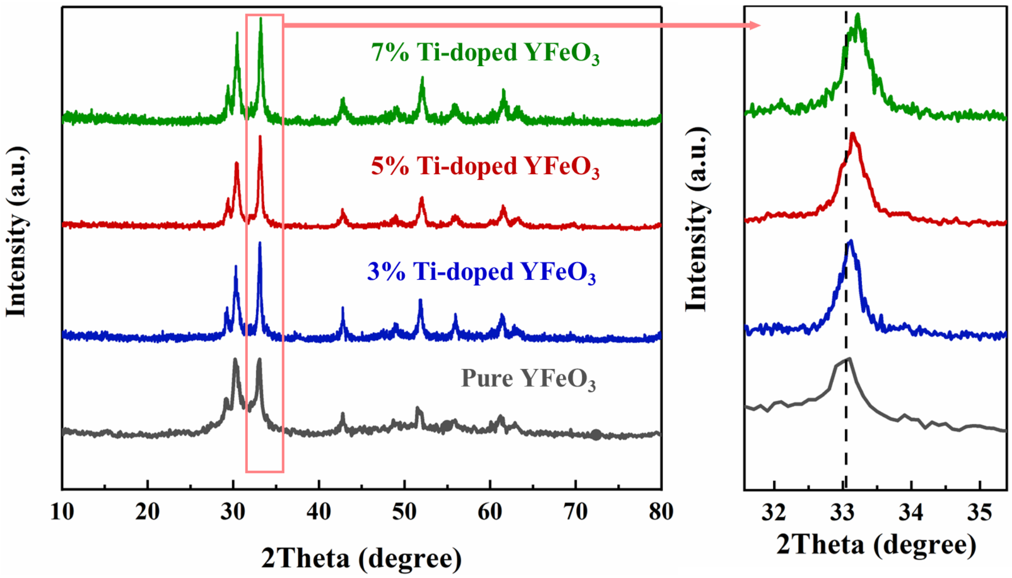

Fig. S3. XRD patterns of YFeO$_3$ with different Ti doped ratios.

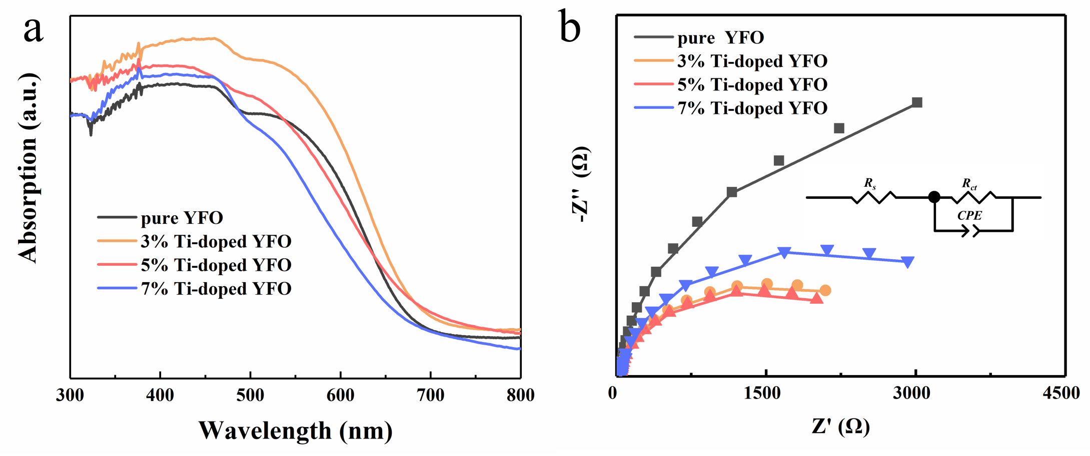

Fig. S4. (a) Light harvesting efficiency spectra for $YFeO_3$ with different Ti doped ratios. (b) Electrochemical impedance spectra (EIS) of pure $YFeO_3$, 3%, 5% and 7% Ti-doped $YFeO_3$ in a 1 M NaOH electrolyte at 1.6 V vs RHE. The right inset is an equal circuit for the catalyst/electrolyte interfaces. Electrochemical impedance spectrum fitting result is shown in Table S3. R_s is the electrolyte resistance. R_{ct} and *CPE* is the charge-transfer resistance from the bulk to the surface of catalyst and the constant phase element, respectively.

Fig. S4 showed the photo-absorption curve of pure $YFeO_3$, 3%, 5% and 7% Ti-doped $YFeO_3$. $YFeO_3$ showed good light harvest and absorption capacity[1]. The cutoff wavelength of $YFeO_3$ could reach about 700 nm.

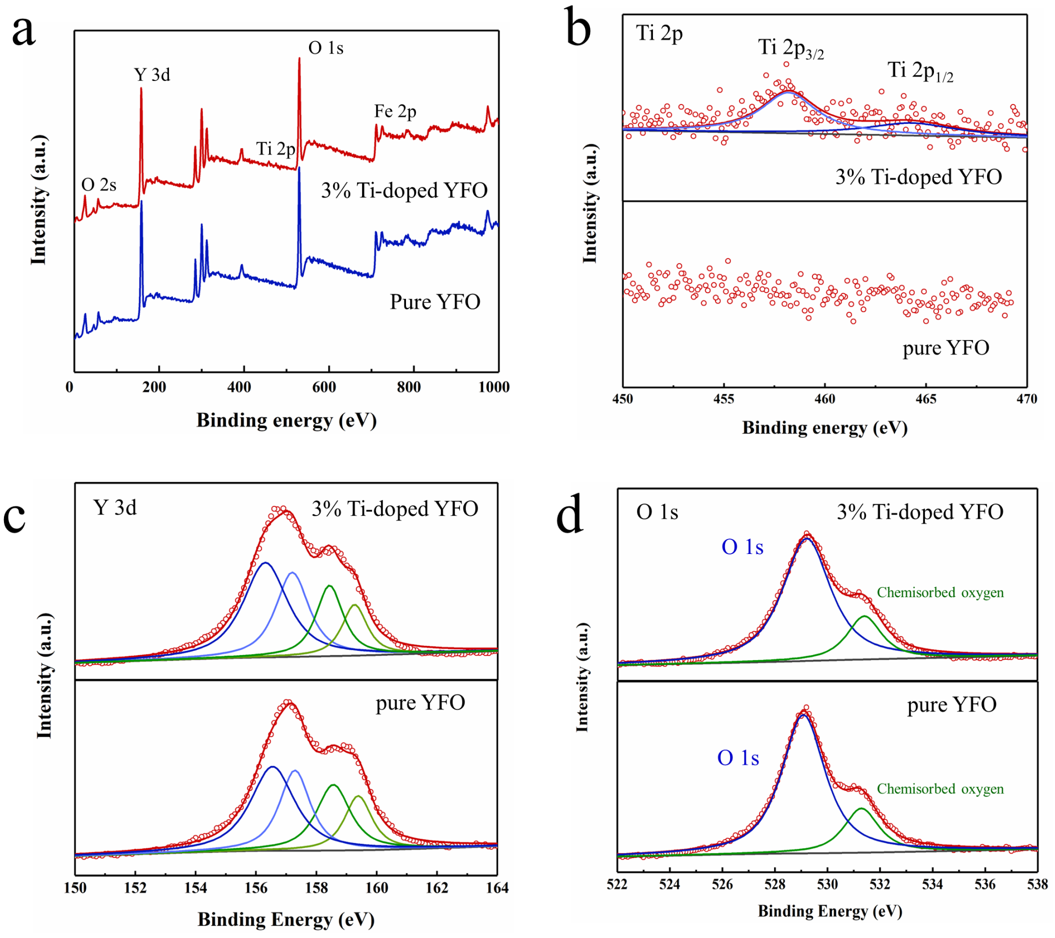

Fig. S5. XPS survey spectra. (a) XPS survey spectra of pure $YFeO_3$ and 3% Ti-doped $YFeO_3$ from 0 to 1000 eV. XPS spectra of pure $YFeO_3$ and 3% Ti-doped $YFeO_3$: (b) Ti 2p, (c) Y 3d, (d) O 1s

Fig. S5a showed the XPS survey spectra of pure $YFeO_3$ and 3% Ti-doped $YFeO_3$ from 0 to 1000 eV. Fig. S5c showed the high-resolution Y 3d region with two spin-orbit doublets with the main peaks. The Ti 2p region XPS spectra of pure $YFeO_3$ and 3% Ti-doped $YFeO_3$ were distinguished by Fig. S5b. There were two signals in the spectra of 3% Ti-doped $YFeO_3$ located at 458.2 eV and 464.3 eV corresponding to Ti 2p3/2 and Ti 2p1/2, which was agreed with the reported date[2]. It meant the doped Ti ions were presented as Ti^{4+} species. Fig. S5d showed the O 1s XPS spectra. At lower binding energy represent the oxygen in lattice and the surface absorbed oxygen observed at higher binding energy. The shift of O 1s peak to higher energy after Ti doping again proved that Ti element successfully entered the lattice of $YFeO_3$.

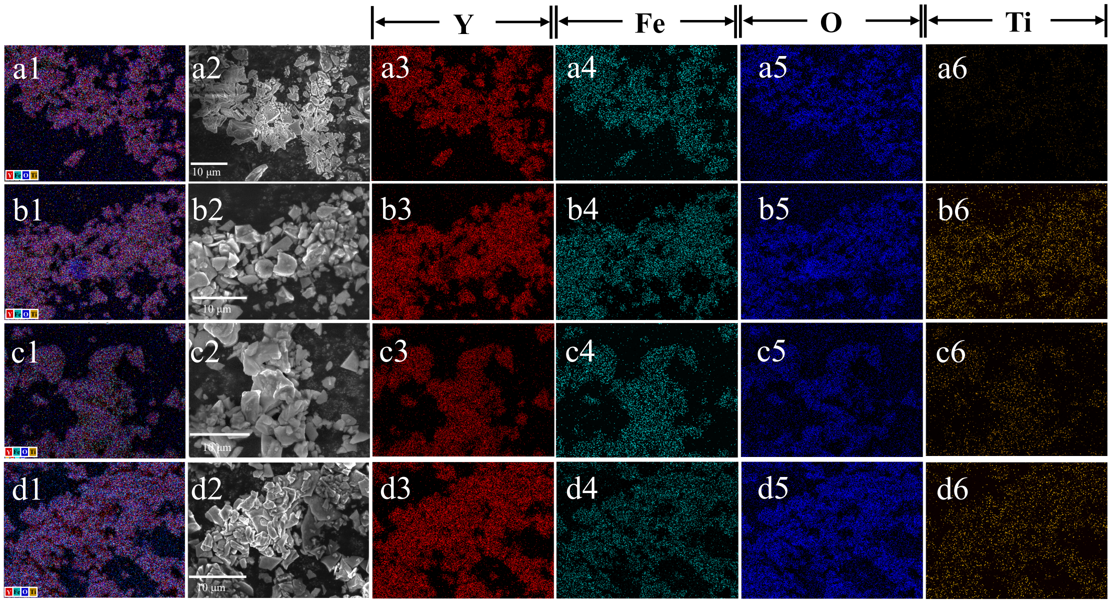

Fig. S6. SEM and EDS images. (a) $YFeO_3$, (b) 3% Ti-doped $YFeO_3$, (c) 5% Ti-doped $YFeO_3$, (d) 7% Ti-doped $YFeO_3$.

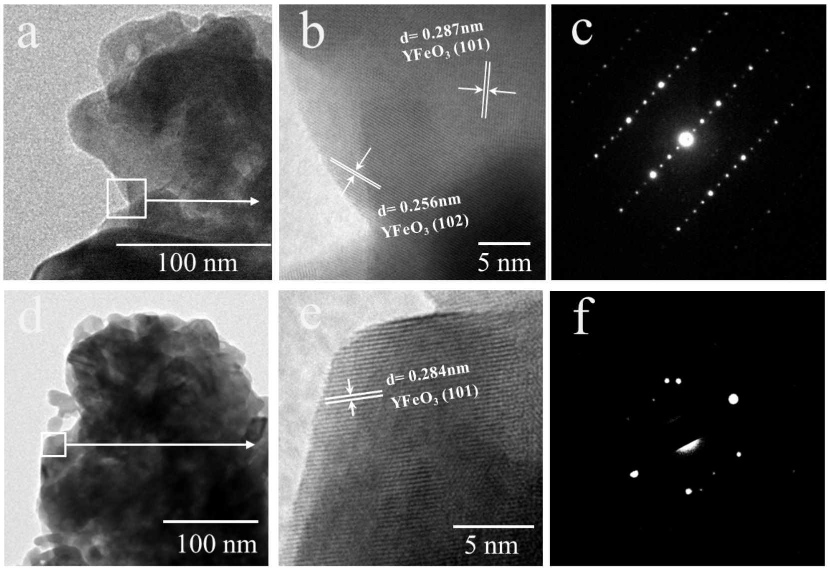

Fig. S7. TEM images. Low-resolution TEM of (a) $YFeO_3$, (d) 3% Ti-doped $YFeO_3$. In the high-resolution TEM images, the lattice spacings of (b) $YFeO_3$, (e) 3% Ti-doped $YFeO_3$ are visible. Electron diffraction spot of (c) $YFeO_3$, (f) 3% Ti-doped $YFeO_3$

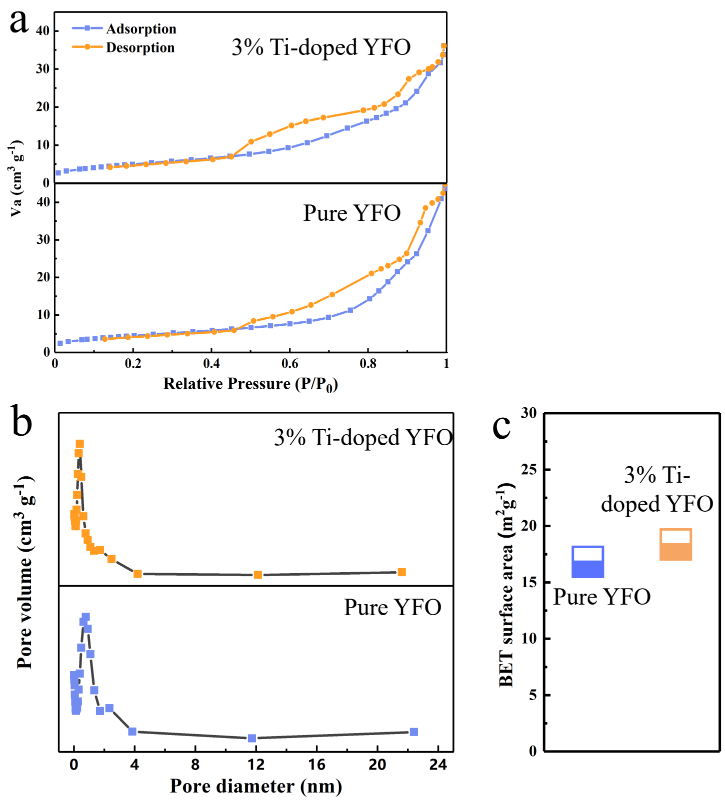

Fig. S8. The specific surface area and pore size distributions of the samples. (a) Nitrogen adsorption-desorption isotherms. (b) Pore size distribution based on BJH model. (c) The BET surface areas of pure and 3% Ti-doped YFeO$_3$.

The specific surface area and pore size distributions of the samples were measured using the BET method. As noted in Supplementary Fig. 8a the isotherms were classified as type IV with H$_2$ hysteresis loops (0.5–1 P/P$_0$) according to the International Union of Pure and Applied Chemistry (IUPAC) classification and the specific surface area of 3% Ti-doped YFeO$_3$ reached 18.38 m^{2}g^{-1}, similarly to that of pure YFeO$_3$ (16.81 m^{2}g^{-1}) (Fig. S8c).

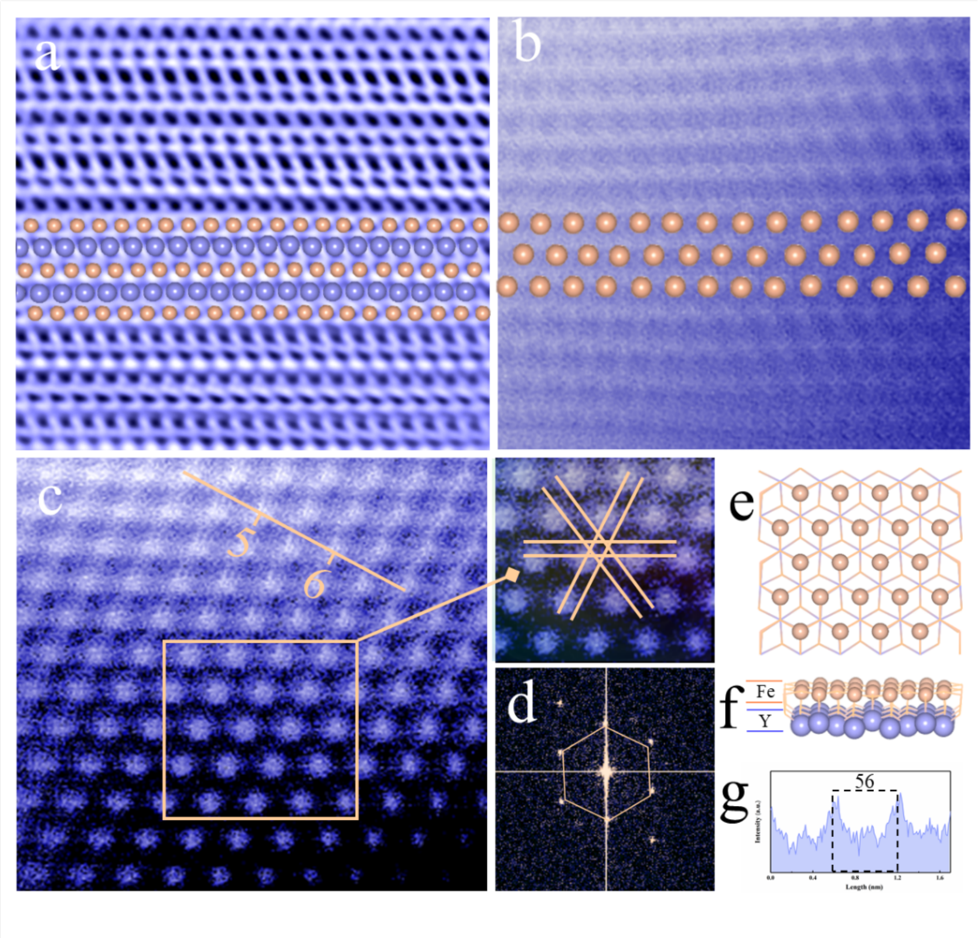

Fig. S9. Spherical aberration-corrected scanning transmission electron (STEM) images. (a, b) annular bright field (ABF) image of pure $YFeO_3$ and Ti-$YFeO_3$ and (c) high-angel annular dark field (HADDF) image of Ti-$YFeO_3$. (The right is the selected area of the left.) The scale bars are 1nm. (d) The corresponding fast Fourier transform (FFT) patterns of Ti-$YFeO_3$. (e) The crystal structure model of (001) plane and (f) perpendicular to the (001) plane. (g) Profile of the line in (c). The yellow and blue spheres represent Fe and Y atoms.

.

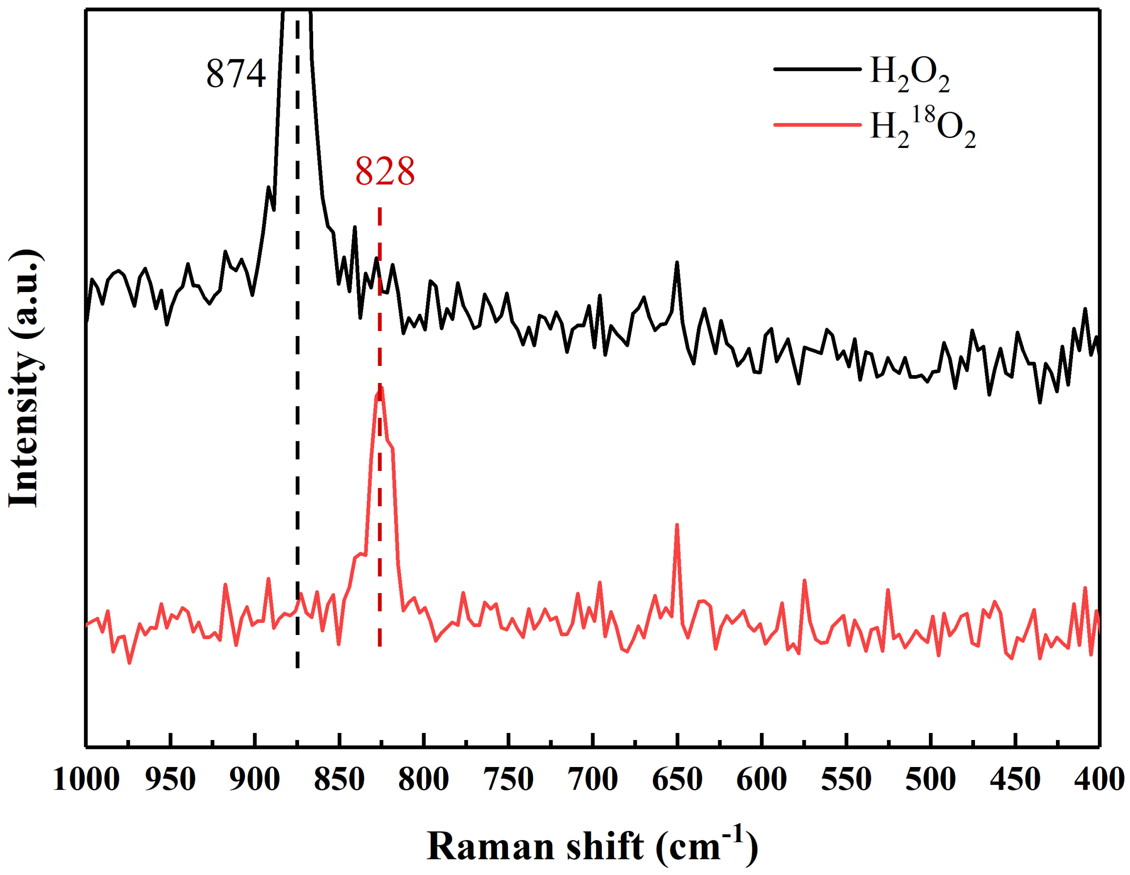

Fig. S10. Shell-isolated nanoparticle-enhanced Raman spectroscopy of H_2O_2 (3 wt.% H_2O_2/H_2O) and $H_2{}^{18}O_2$ (^{18}O isotope labelling, 2-3 wt.% $H_2{}^{18}O_2/H_2O$).

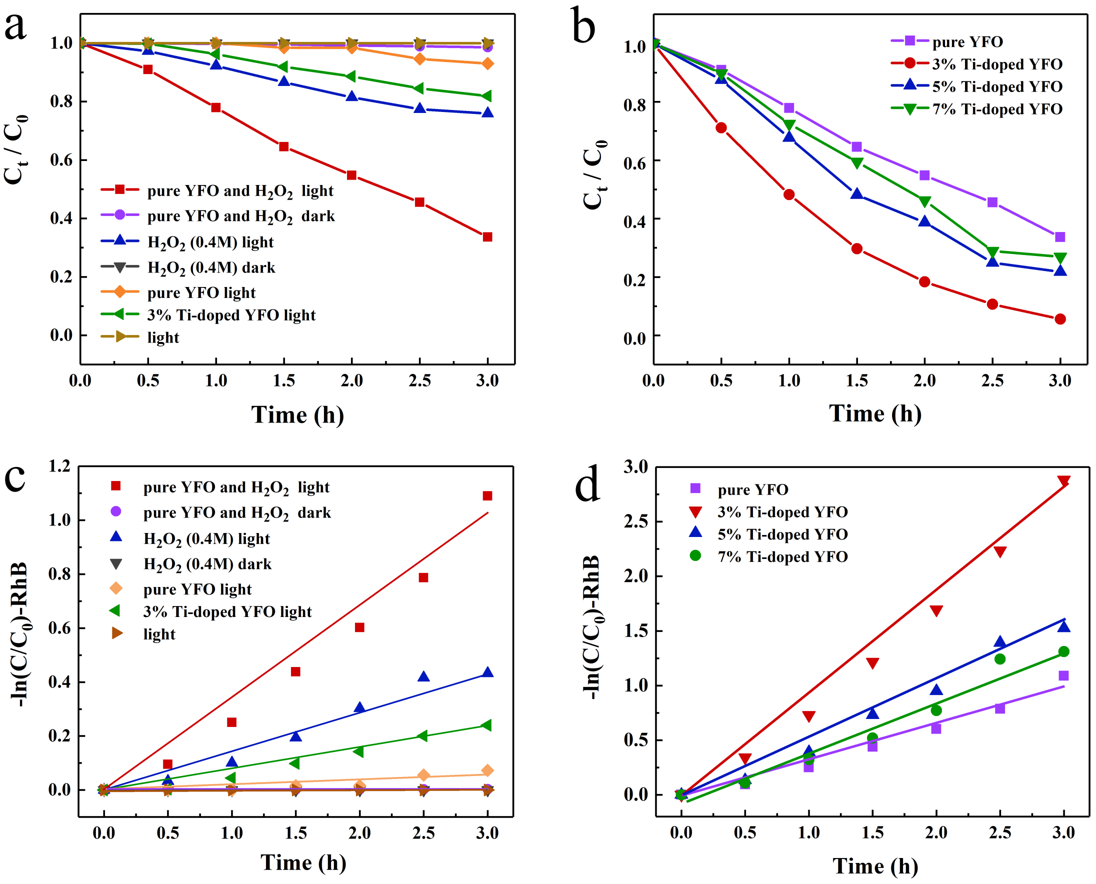

Fig. S11. Photo-Fenton reaction performance. (a) Time dependent RhB solution degradation in different systems. Specially, in pure $YFeO_3$ light and 3% Ti-doped $YFeO_3$ light systems, there were no H_2O_2. (b) Time dependent RhB solution degradation for pure $YFeO_3$ and 3%, 5%, 7% Ti-doped $YFeO_3$ with H_2O_2. (c, d) the corresponding Langmuir-Hinshelwood kinetics plots in these systems.

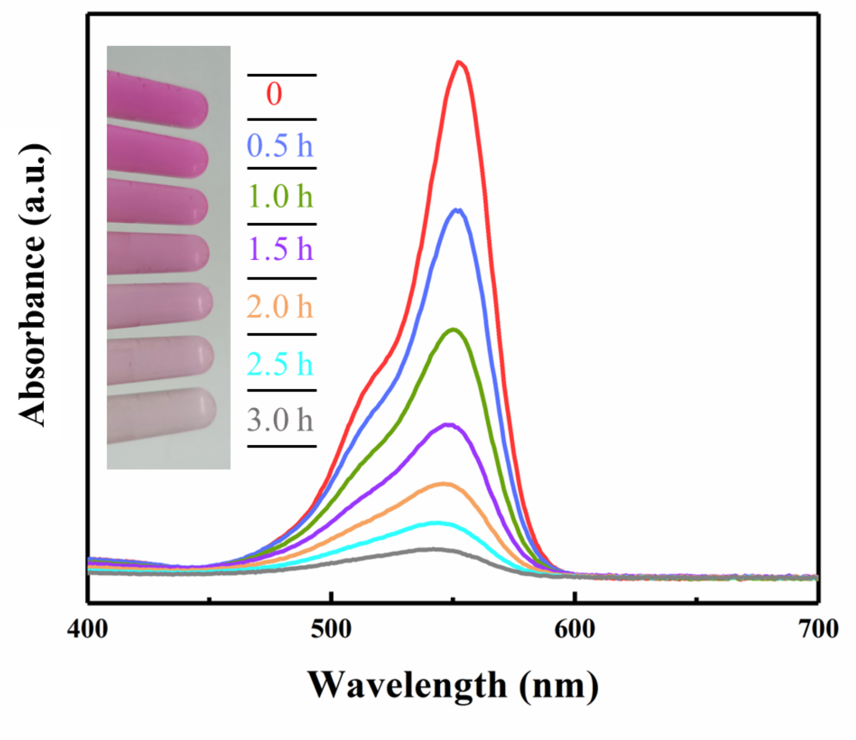

Fig. S12. UV–vis spectral changes for RhB degradation with Ti-$YFeO_3$/H_2O_2/light system.

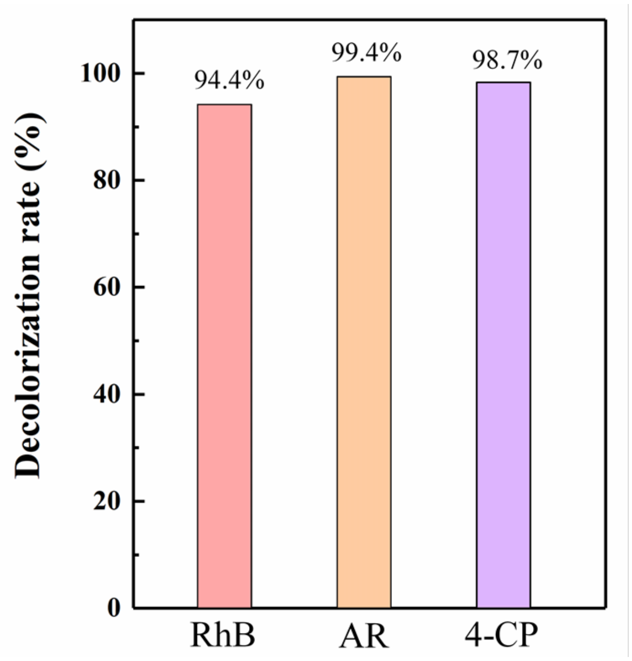

Fig. S13. The removal efficiencies of different pollutants after reacting for 3 h.

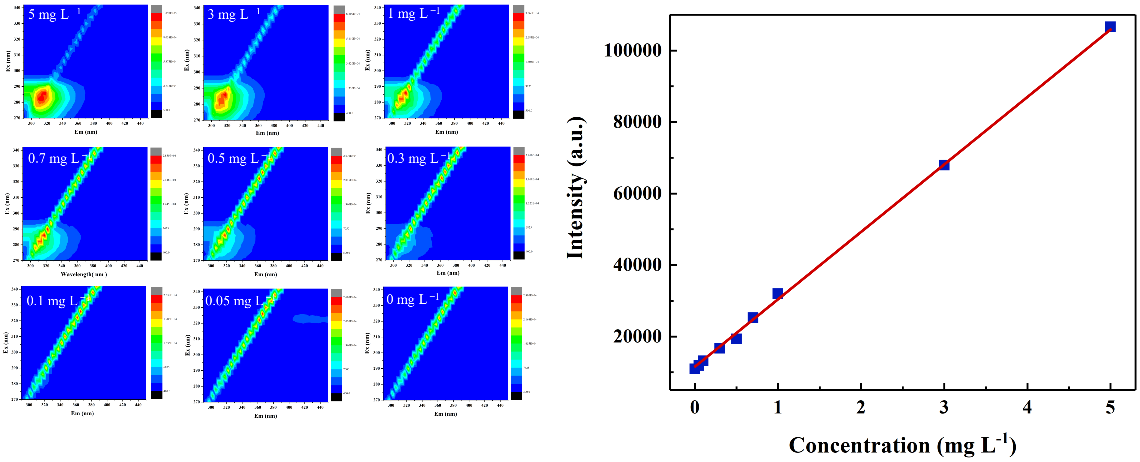

Fig. S14. Calibration curve of 4-CP for 3-dimension excitation emission matrix fluorescence spectroscopy (3D-EEM). The left part showed 3D-EEM of 4-CP aqueous solutions with different concentrations (0 to 5 mg L^{-1}). The excitation range was 270 to 340 nm, and the emission range was 290 to 450 nm. The right part showed that 3D-EEM intensity of 4-CP aqueous solutions had a linear relationship with the concentrations.

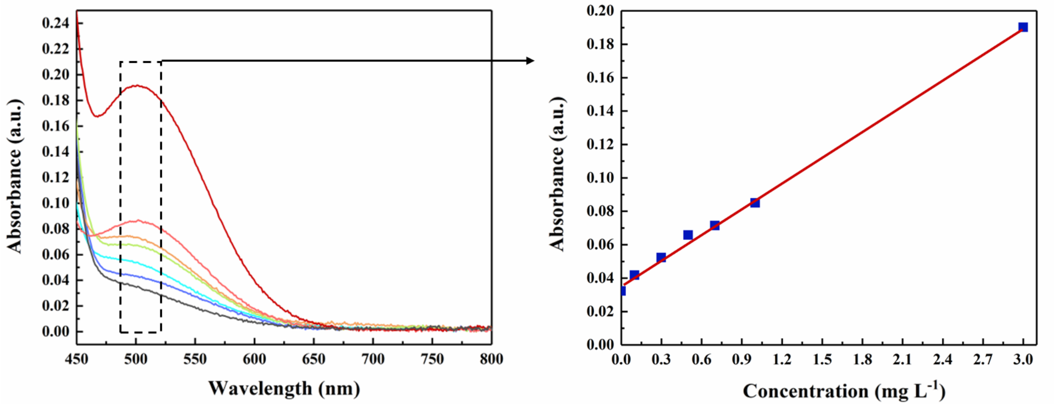

Fig. S15. Calibration curve under 4-aminoantipyrine methods. The left part showed the light absorption curves of 4-CP solutions with different concentrations (0 to 3 mg L^{-1}) under the test of 4-aminoantipyrine methods. The right part showed that light absorption intensity of 4-CP aqueous solutions had a linear relationship with the concentrations.

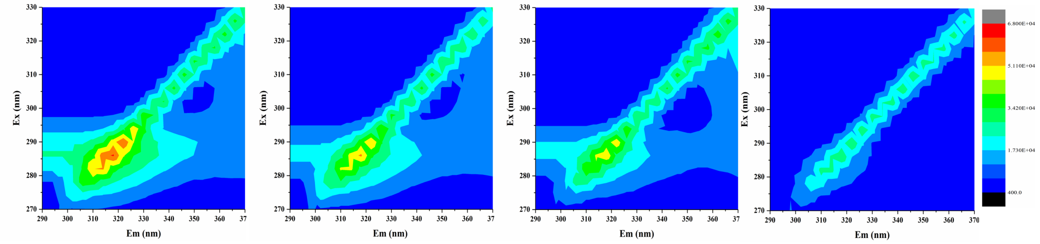

Fig. S16. 3D-EEM fluorescence spectra of 4-CP after different time degradation. (From left to right: 0 min, 30min, 90min, 180min.)

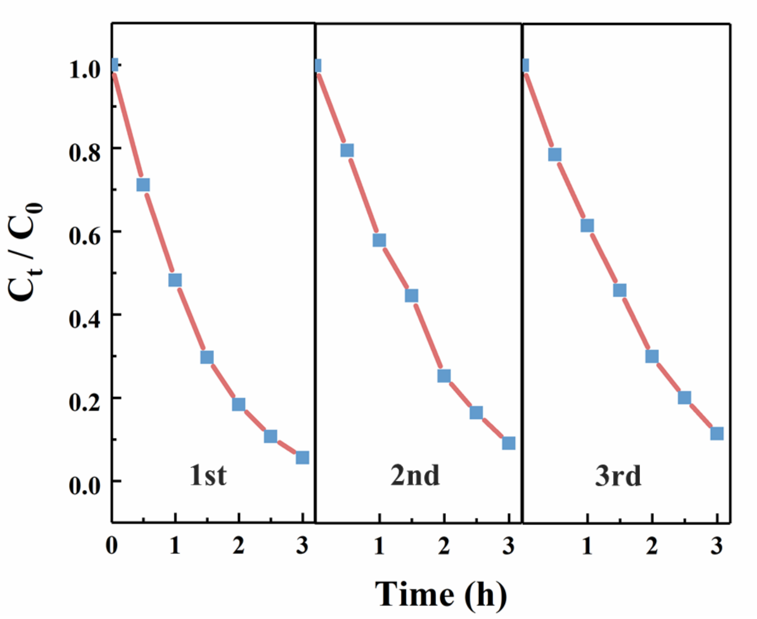

Fig. S17. Degradation efficiencies of RhB in Ti-$YFeO_3$/H_2O_2 light system with 3-round reactions.

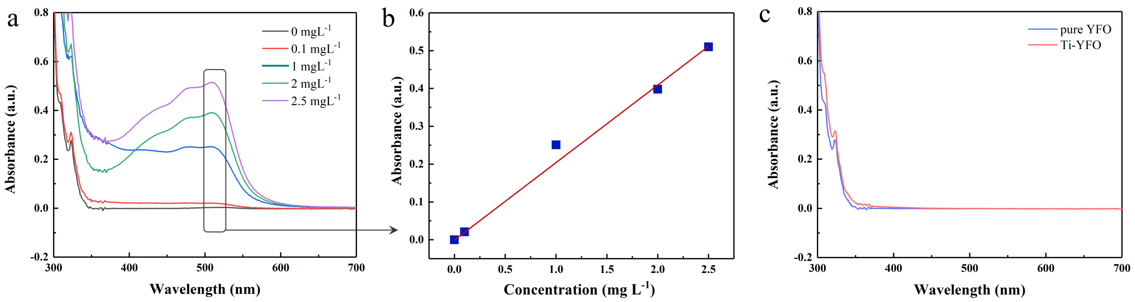

Fig. S18. Calibration curves of Fe^{3+} ions under the 1, 10-phenanthroline method and detection curves of Fe^{3+} ions for the different systems. (a) The light absorption curves with different-concentration Fe^{3+} ions under the test of 1, 10-phenanthroline methods. (b) The light absorption intensity had a linear relationship with the concentrations. (c) Absorptance curves of Fe^{3+} ions in the solution after reaction for pure $YFeO_3$ and Ti-$YFeO_3$ under the 1, 10-phenanthroline method.

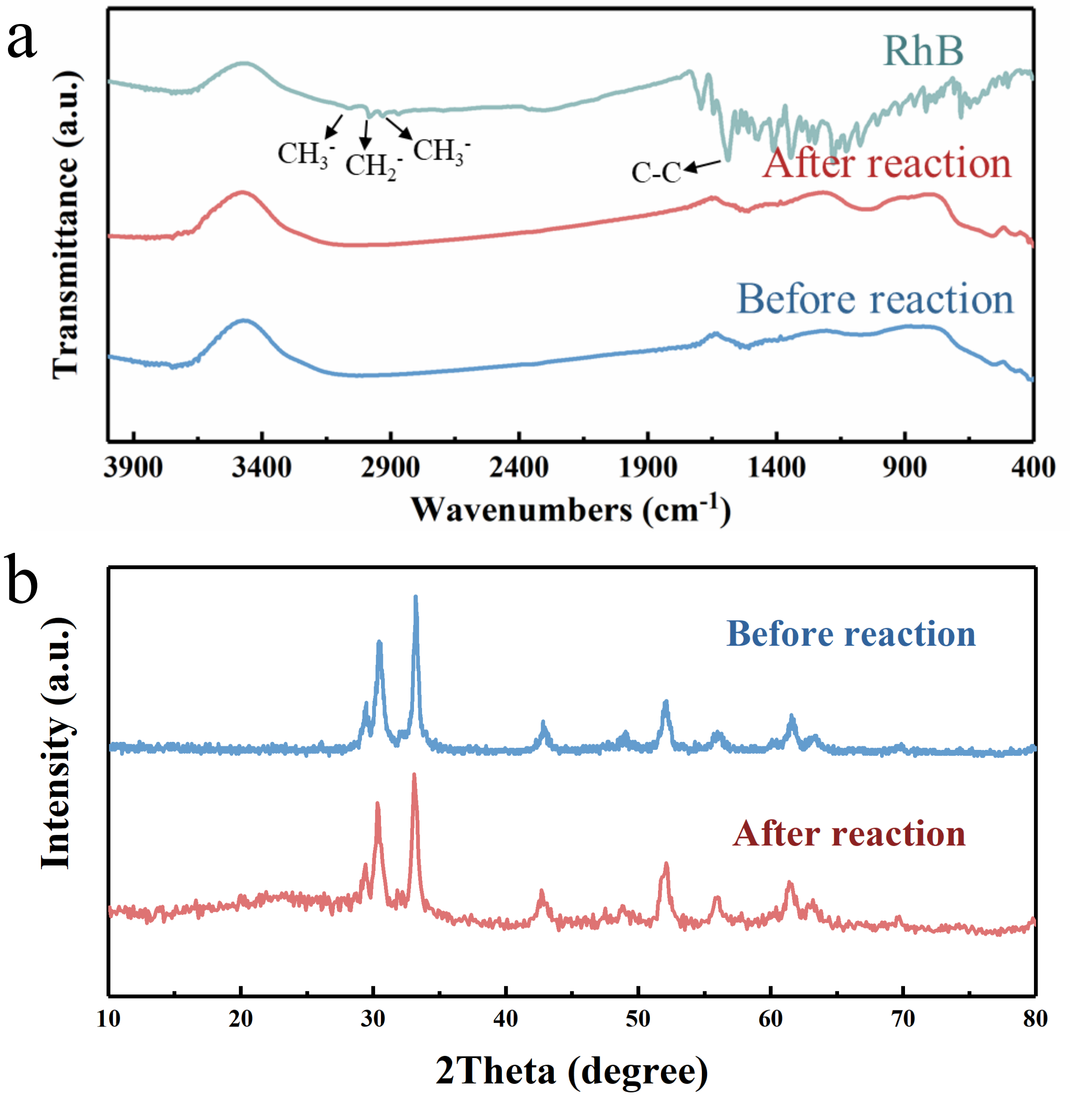

Fig. S19. Characterization of catalysts before and after reaction. (a) Fourier translation infrared spectroscopy (FT-IR) and (b) XRD of Ti-YFeO$_3$ before and after reaction.

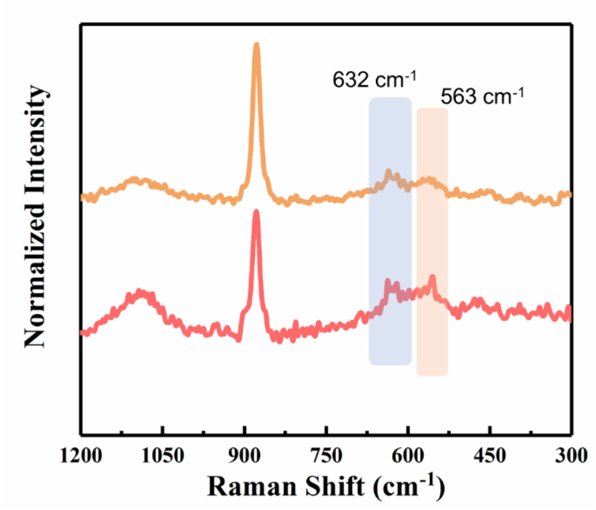

Fig. S20. Shell-isolated nanoparticle-enhanced Raman spectroscopy (SHINERS) with H_2O_2 in different system. (Yellow: $YFeO_3$ system and Red: Ti-$YFeO_3$ system)

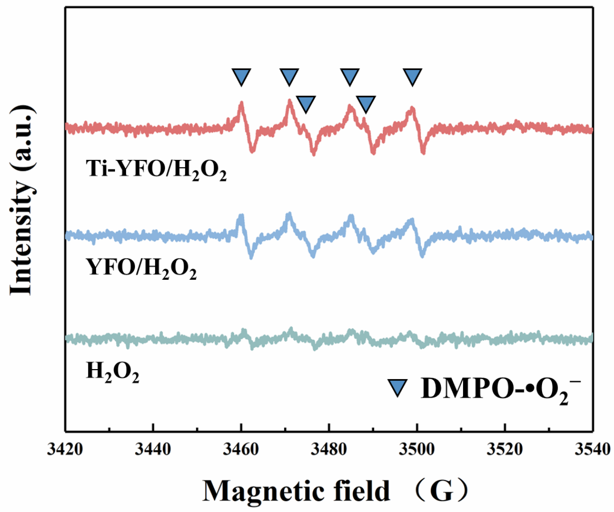

Fig. S21. DMPO-•O_2^- for different systems after 15-minute visible light irradiation, respectively.

Furthermore, it was clear that •OH free radical was the main active species, but how it acts on pollutants was unclear. In order to study the method of •OH active free radicals working in the process of pollutant explanation, the degradation products of the model compound 4-chlorophenol were analyzed by electrospray high resolution mass spectrometry (ESI-HRMS) analysis (Fig. S22 and S23) in negative ion mode (ESI), and the proposed molecular transformation pathways were inferred (Fig. 4g). Initial substrate 4-chlorophenol (deprotonated excimer ion peak m/z 127 by ionization in ESI mass spectrometry) was mainly degraded by the substitution, addition, or oxidation reaction of •OH active species and its degradation pathway mainly showed three reaction channels. The first reaction channel (down): 4-chlorophenol was oxidized dechlorination atom to form hydroquinone by •OH active species and then, the ring-opening cracking of benzene ring was induced by further oxidation to produce small carboxylic acids such as acetic acid, glycolic acid, buteneic acid and so on. These molecules finally were oxidized and degraded to generate small molecules of H_2O, CO_2, H_2CO_3, etc. The second and third reaction channels (up) were continuous oxidation of benzene ring followed by oxidative dechlorination. 4-chlorophenol was oxidized to 4-Chlorobenzene-1,2-diol by substituting the hydrogen on the benzene ring with the •OH active species. 4-Chlorobenzene-1,2-diol was continue oxidized to form dihydroxy-tetrachlorophenol and then was oxidized dechlorination (channel 3). 4-Chlorobenzene-1,2-diol was directly oxidized dechlorination to form phloroglucinol (channel 2). The benzene rings of these molecules were broken down through the addition reactions, causing them to be degraded into small carboxylic acids. And they finally were degraded to generate small molecules. In terms of the response strength of the products (Fig. 4g) obtained from the three different paths, the first and second paths were more favorable than the third one, which may be due to the highest Fukui index values of the chlorine groups in 4-chlorophenol's structure, leading to their preference for •OH species' attacking[3]. As a result, the degradation of p-chlorophenol molecules was more prone to dechlorination followed by oxidation and deep cracking of the benzene ring.

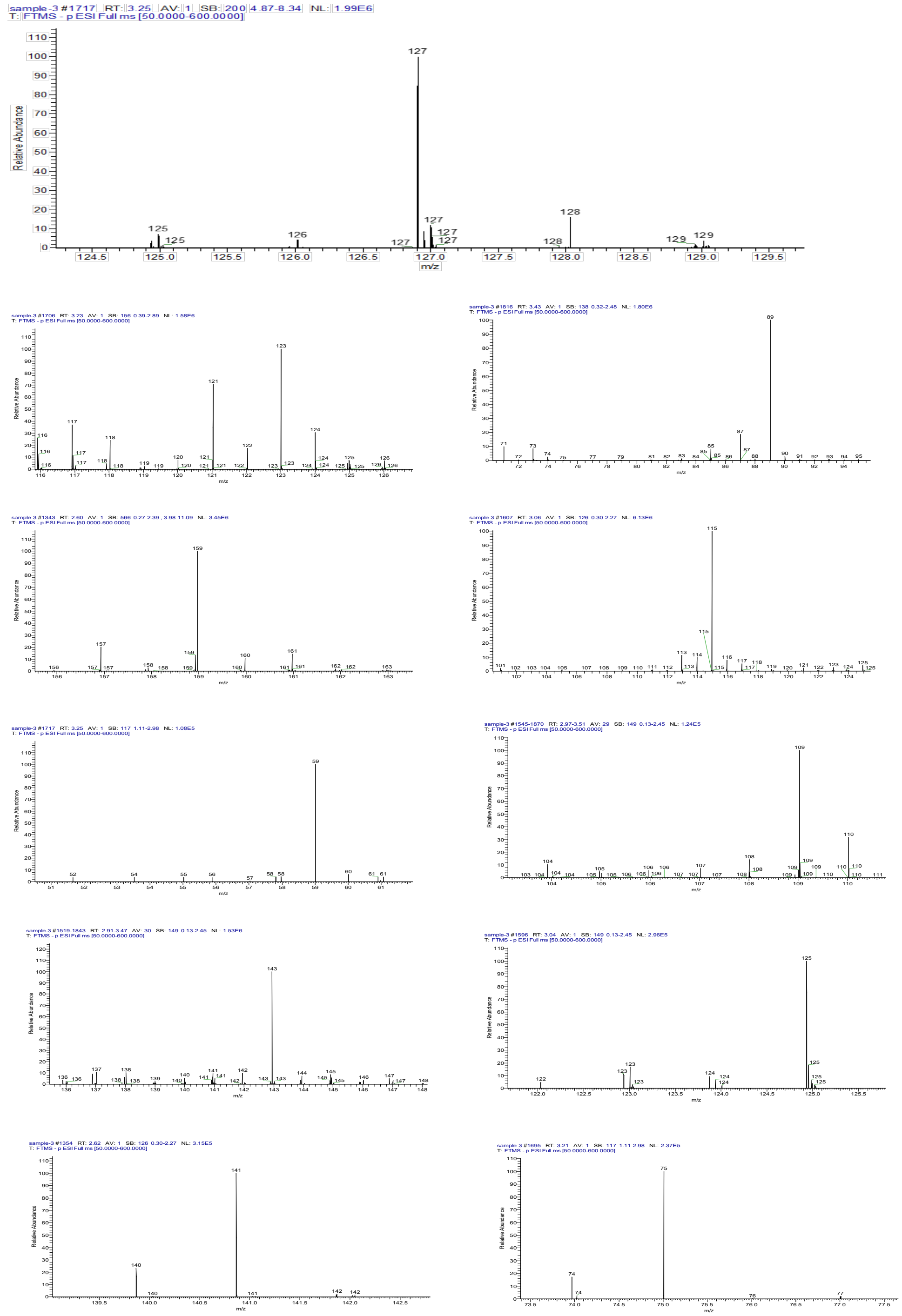

Fig. S22. Mass spectrum of 4-CP decomposition intermediate products.

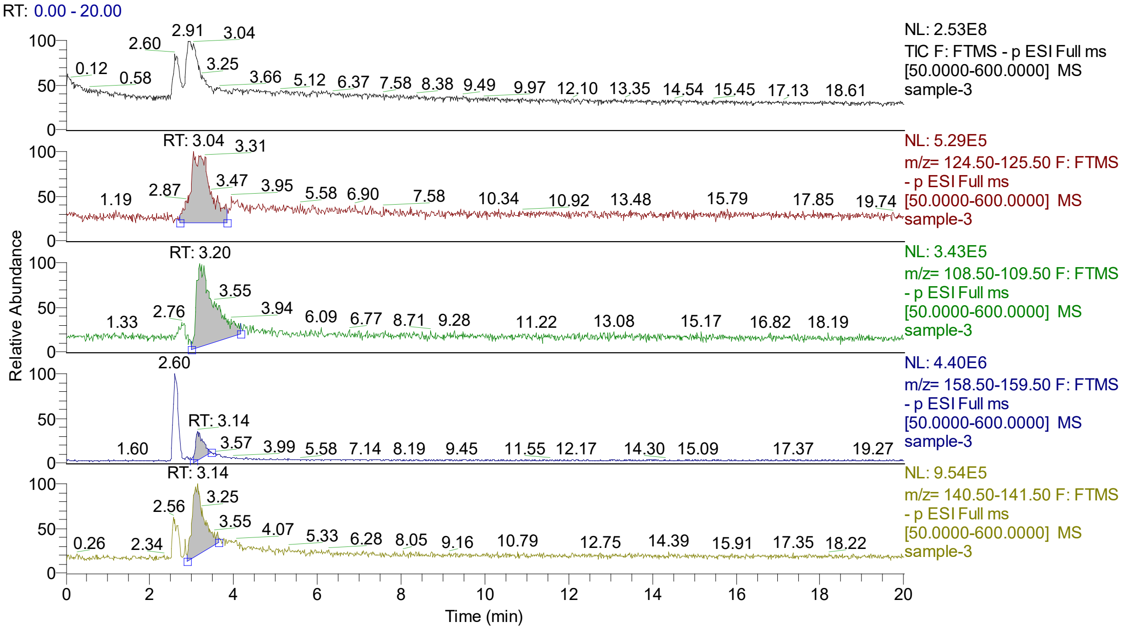

Fig. S23. GC-MS information at 30 minutes. The chromatographic images and mass spectrometry information were shown on the left and right, respectively. At 30 minutes of reaction, $C_6H_5O_3^-$ (m/z=125.02), $C_6H_5O_2^-$ (m/z=109.03), $C_6H_4ClO_3^-$ (m/z=158.99) and $C_6H_5O_4^-$ (m/z=141.02) species appeared. They belonged to channel 2, 1, 2 and 3, respectively. According to their integral strength, channel 1 and 2 as the intermediate species may play dominant roles.

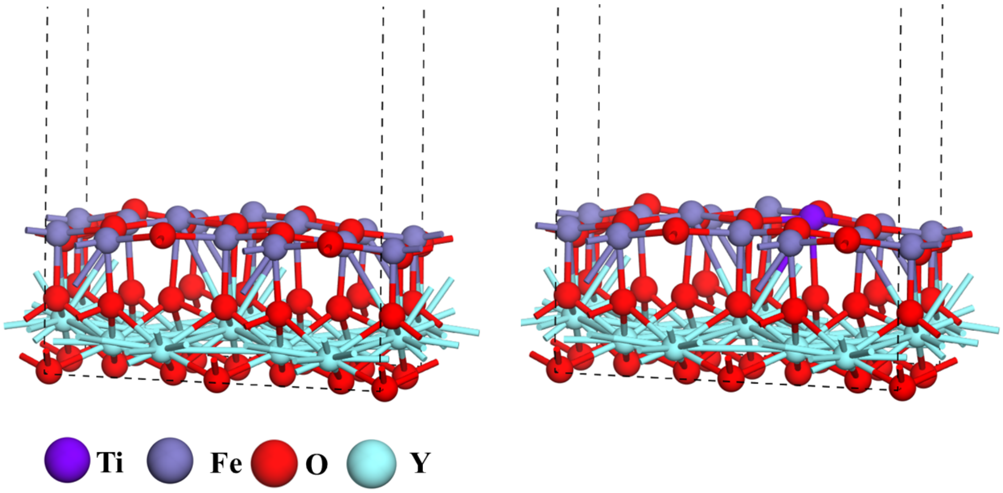

Fig. S24. The structure of $YFeO_3$ and Ti-$YFeO_3$.

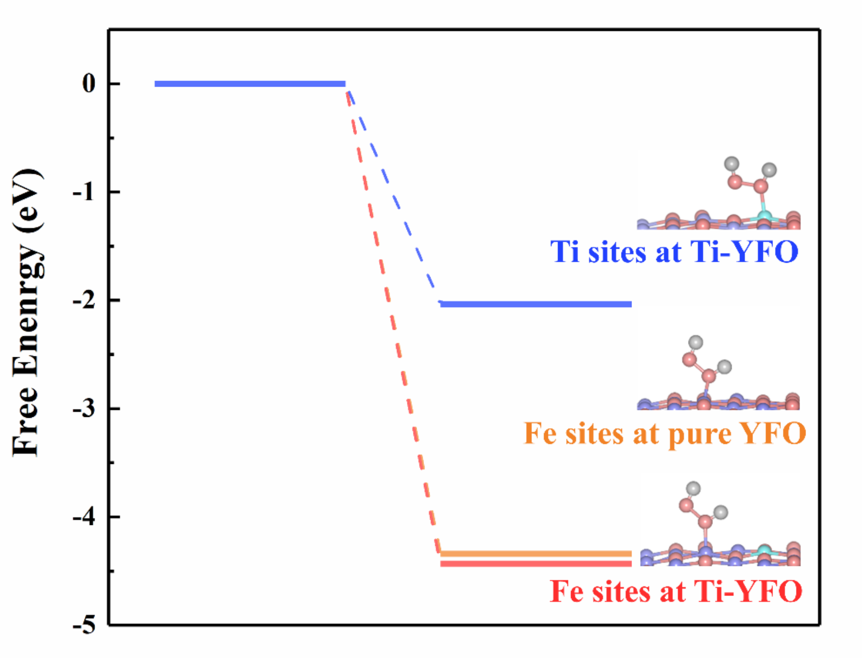

Fig. S25. Calculated H_2O_2 adsorption energy profiles for Ti sites at Ti-$YFeO_3$ (blue), Fe sites at pure $YFeO_3$ (yellow) and Fe sites at Ti-$YFeO_3$ (red).

Table S1. EXAFS fitting parameters at the Fe K-edge for $YFeO_3$ and Ti-$YFeO_3$.

Sample	**Shell**	**N[a]**	**R(Å)[b]**	**σ^2(Å^2)[c]**	**R factor**
$YFeO_3$	Fe-O	5.10	2.12	0.00464	0.018
$YFeO_3$	Fe-Fe	6.01	3.63	0.00536	0.018
Ti-$YFeO_3$	Fe-O	5.11	2.14	0.00476	0.010
Ti-$YFeO_3$	Fe-Fe	6.05	3.66	0.00787	0.010

[a]N: coordination numbers; [b]R: bond distance; [c]σ^2: Debye-Waller factors; R factor: goodness of fit.

Table S2. Calculated free energy dates for the decomposition Path I and Path II of H_2O_2 moles on the surface of $YFeO_3$ and Ti-$YFeO_3$. (The unit is eV.)

Sample	H_2O_2	*H_2O_2	H-OOH(TS)	*OOH+H	*OH	•OH
$YFeO_3$	0	-4.34192	-3.26166	-4.81457	-3.413	-2.46
Ti-$YFeO_3$	0	-4.43154	-4.03154	-4.69154	-3.20034	-2.46
Sample	**H_2O_2**	***H_2O_2**	**HO-OH(TS)**	***OH+OH**	***OH**	**•OH**
$YFeO_3$	0	-4.34192	-2.9351	-4.8143	-3.413	-2.46
Ti-$YFeO_3$	0	-4.43154	-3.45461	-4.5143	-3.20034	-2.46

Table S3. Electrochemical impedance spectrum fitting result in Fig.S4b.

	R_s **(Ω)**	***R_{ct}*** **(Ω)**	***CPE-T*** **(F)**	***CPE-P*** **(F)**
Pure YFO	38.09	**9387**	7.071E-06	0.968
3% Ti-doped $YFeO_3$	38.74	**2969**	9.838E-06	0.961
5% Ti-doped $YFeO_3$	38.49	**2731**	1.003E-06	0.959
7% Ti-doped $YFeO_3$	45.6	**4037**	6.815E-06	0.971

SI References

1. Y. S. Guo *et al.*, A novel wide-spectrum response hexagonal $YFeO_3$ photoanode for solar water splitting. *RSC Adv.* 7, 18418-18420 (2017).
2. M. Ismael *et al.*, Synthesis of phase pure hexagonal $YFeO_3$ perovskite as efficient visible light active photocatalyst. *Catalysts* 7, 326 (2017).
3. F. Li *et al.*, Hydrothermal synthesis of graphene grafted titania/titanate nanosheets for photocatalytic degradation of 4-chlorophenol: Solar-light-driven photocatalytic activity and computational chemistry analysis. *Chem. Eng. J.* 331, 685-694 (2018).